Composites Part B 323 (2026) 113777

Contents lists available at ScienceDirect

Composites Part B

journal homepage: www.elsevier.com/locate/compositesb

Genetic-algorithm-optimized honeycomb-reinforced metamaterial aerogel for broadband microwave absorption

Zibo Li [a], Zhichun Zhang [a,*], Anping Wang [a], Yanju Liu [b], Jinsong Leng [a,**]

[a] Centre for Composite Materials and Structures, Harbin Institute of Technology (HIT), Harbin, 150080, People's Republic of China
[b] Department of Astronautic Science and Mechanics, Harbin Institute of Technology (HIT), Harbin, 150001, People's Republic of China

ARTICLE INFO

Keywords:
Metamaterial aerogel
Aramid honeycomb
Genetic algorithm
Electromagnetic wave absorption
Mechanical performance

ABSTRACT

Aerogel absorbers are attractive for lightweight electromagnetic wave attenuation, but their structural brittleness and limited geometric stability remain major constraints for engineering use. Simultaneously improving mechanical robustness and broadband absorption remains challenging. Here, we present a metamaterial aerogel composite that integrates mechanical reinforcement with broadband electromagnetic wave absorption. A parametric unit-cell model, governed by four coupled geometric variables, was constructed to span a continuous family of shapes from uniform slab through frustum to pyramid. A genetic algorithm searched this multi-dimensional design space to maximize effective absorption bandwidth (EAB) over 2–18 GHz under a 10 mm thickness constraint, converging on an optimized frustum configuration. The optimized geometry was fabricated as a polyimide/multi-walled carbon nanotube metamaterial aerogel (PCMA) and further integrated with aramid honeycomb to form the corresponding polyimide/multi-wall carbon nanotube (PI/CNT) metamaterial aerogel composite (PCMAC) by in-situ infiltration, freeze-drying, and thermal imidization. Mechanical tests further show that PCMAC-9.6 reaches compressive and nominal flexural strengths of 4.3 MPa and 0.80 MPa, respectively, exceeding both the empty honeycomb and the pure PCMA control. Compared with pure PCMA, PCMAC-9.6 exhibits an approximately 70–80% higher compressive strength and more than fourfold higher nominal flexural strength. These results demonstrate a practical route to multifunctional composites that combine broadband absorption with load-bearing capability for aerospace applications.

1. Introduction

With the rapid development of electronic devices, electromagnetic (EM) interference has become a growing concern for both device reliability and information security [1–4]. High-performance microwave absorption (MA) materials are therefore required to mitigate undesired EM radiation. Conventional absorbers are commonly implemented as coating layers [5–7], yet their relatively high density limits use in weight-sensitive applications [8]. Aerogels are attractive alternatives because their three-dimensional porous networks provide ultralow density and abundant internal interfaces that promote multiple scattering and attenuation of incident EM waves [9–11].

Although aerogels offer these structural advantages, most aerogel absorbers are compositionally homogeneous, which often leads to imperfect impedance matching and limited absorption bandwidth [12–14]. To broaden the operating band, spatial concentration gradients and other compositional modulations (for example, graded filler loading or multilayer laminates) have been explored [15–18]. However, generating controlled heterogeneous profiles typically relies on stepwise, layer-by-layer processing of precursor solutions, which demands tight control over local filler distribution and is vulnerable to interfacial defects and batch-to-batch variability [19–23]. These practical constraints hinder translation from laboratory demonstrations to structurally consistent engineering components.

Metamaterials provide an alternative design route in which broadband response is primarily engineered through geometry, reducing dependence on intrinsic material dispersion [24–26]. In particular, metamaterials can smooth the impedance transition from free space into the absorber by varying unit-cell geometry along the thickness direction [27–29]. Conventionally, the unit-cell geometry is determined by sweeping one variable at a time while keeping the other fixed, or by comparing a small number of predefined shapes [30–32]. Such

* Corresponding author.
** Corresponding author.
E-mail addresses: zczhang@hit.edu.cn (Z. Zhang), lengjs@hit.edu.cn (J. Leng).

https://doi.org/10.1016/j.compositesb.2026.113777
Received 21 March 2026; Received in revised form 26 April 2026; Accepted 5 May 2026
Available online 6 May 2026

single-variable approaches can identify locally favorable configurations but are limited when the search space involves several strongly coupled geometric parameters, since they do not explore the joint design space globally. Hence, a parametric unit-cell model coupled with a genetic algorithm (GA) [33] is used here to optimize the metamaterial geometry within a constrained design space. The model spans a continuous range of slab-to-pyramid configurations, and the simultaneous adjustment of all geometric variables enables the multi-dimensional design space to be searched for a structure that maximizes EAB across 2–18 GHz under fixed-thickness and manufacturability constraints.

Although metamaterials can enhance electromagnetic performance, aerogels remain mechanically fragile and prone to processing-induced distortion, which restricts their use in load-bearing structures [34–36]. Aramid honeycomb (AH) is widely used as a lightweight reinforcement due to its high specific stiffness and established aerospace manufacturability. However, conventional AH-reinforced aerogel composites often adopt uniform filling, where honeycomb cells are fully filled with a homogeneous absorber [37–40]. This configuration improves mechanical robustness but can reintroduce a sharp impedance discontinuity at the air–material interface and reduce tunability, leading to strong surface reflection and constrained bandwidth.

In this work, a parametric unit-cell model governed by four coupled geometric variables is constructed and combined with a genetic algorithm to optimize the metamaterial geometry through full-wave electromagnetic simulation (CST Microwave Studio). The GA searches a continuous design space spanning slab-to-pyramid configurations and converges on a frustum-based PI/CNT metamaterial aerogel, denoted as PCMA, that maximizes EAB over 2–18 GHz under a fixed thickness of 10 mm. On this optimized basis, the PCMA structure is integrated with aramid honeycomb to form the corresponding PI/CNT metamaterial aerogel composite, denoted as PCMAC. The influence of AH cell size on the electromagnetic response of PCMAC is systematically investigated. Experimental measurements of both PCMA and PCMAC are conducted to compare their broadband absorption performance and mechanical load-bearing capacity. The results evaluate the influence of honeycomb cell size on impedance matching and field/loss redistribution around the GA-optimized frustum geometry, and demonstrate the load-bearing improvement introduced by honeycomb-supported aerogel integration.

2. Experimental section

2.1. Materials

4,4′-oxydianiline (ODA, 98%), pyromellitic dianhydride (PMDA, 99%), N,N-dimethylacetamide (DMAc, 99%), and 2-dimethylaminoethanol (DMEA) were obtained from Shanghai Aladdin Biochemical Technology Co., Ltd. Multi-walled carbon nanotubes (CNTs, 10–30 nm in diameter, 10–30 μm in length, 98% purity) were purchased from Chengdu Jiacai Technology Co., Ltd. Aramid honeycomb with a 9.6 mm cell size (supplier-reported density of 0.048 g cm^{-3}; dielectric properties $\varepsilon' \approx 1.6$ and $\varepsilon'' \approx 0$; non-magnetic behaviour $\mu' \approx 1$ and $\mu'' \approx 0$, as specified by the supplier) was purchased from Beijing Avic Composite Materials Technology Co., Ltd. and used as the reinforcement skeleton for composite fabrication. Deionized (DI) water was produced by a water purification system (UPH-IV-5TNP, ULUPURE, China). All chemicals and reagents were of analytical grade and used as received without further purification. The molds used for shaping PCMA and PCMAC were composed of polytetrafluoroethylene (PTFE).

2.2. Synthesis of PI/CNT aerogel

According to a reported method [41], initially, ODA (31.52 g, 0.15741 mol) and DMAc (300 g) were added into a 500 mL three-neck round-bottom flask fitted with a mechanical stirrer. Once the ODA was completely dissolved, the PMDA (34.33 g, 0.15741 mol) was introduced into the solution in ten equal increments at 30-min intervals. ODA and PMDA were polymerized under an inert atmosphere to yield a viscous polyamide acid (PAA) solution after 8 h of mechanical stirring. The resulting solution was poured into low-temperature deionized water to induce precipitation. The precipitated PAA was washed repeatedly and then freeze-dried to yield a solid PAA precursor. For PI/CNT aerogels, the PAA precursor and DMEA, at a mass ratio of 2:1, were mixed in deionized water at 5 °C under mechanical stirring at 200 rpm for 8 h to form poly(amic acid) salt (PAAs). CNTs were then dispersed in the PAAs solution using a tip-horn ultrasonic processor (LC-1000A, Shanghai Lichen Instrument Technology Co., Ltd., Shanghai, China) operated at 40% amplitude in pulse mode (5 s on/5 s off duty cycle) for a total elapsed run time of 8 h, corresponding to a cumulative on-time of 4 h, with the dispersion vessel held in an ice-water bath at approximately 5 °C to suppress sonication-induced heating. The ultrasonic processor was equipped with temperature control; sonication was automatically paused when the dispersion temperature exceeded 35 °C and resumed after the temperature decreased below 35 °C. The resulting slurry was cast into PTFE molds and subjected to vacuum defoaming at 5 Pa for 3 min to remove entrapped air bubbles. The samples were subsequently frozen in liquid nitrogen and freeze-dried under approximately 5 Pa using the following programmed temperature schedule: −30 °C for 12 h, −20 °C for 12 h, −10 °C for 12 h, 0 °C for 12 h, 10 °C for 8 h, 20 °C for 8 h, and 30 °C for 8 h, giving a total freeze-drying time of 72 h. Thermal imidization was conducted via a stepwise temperature program (100 °C × 1 h, 150 °C × 1 h, 200 °C × 0.5 h, 250 °C × 0.5 h) to convert PAAs to PI. To adjust the filler ratio of PAAs/CNT composite dispersions, the mass ratio of PAAs to CNT was adjusted, and the resulting samples were denoted as PxCy. Specifically, P corresponds to PAAs, C to CNT, where x and y denote the mass ratios of PAAs and CNT, respectively. Accordingly, three sets of composite dispersions (P3C2, P1C1, and P2C3) were fabricated. The prepared PI/CNT samples were tested for electromagnetic performance by the coaxial method. All material ratios are listed in Table S1.

2.3. Synthesis of PI/CNT metamaterial aerogel (PCMA) and PI/CNT metamaterial aerogel composite (PCMAC)

The PAAs/CNT slurry with the best electromagnetic performance (P2C3) was cast into a customized PTFE mold (Fig. S1(a and b)). The slurry was frozen in liquid nitrogen and freeze-dried using the same programmed pressure and temperature schedule described in Section 2.2, followed by the same stepwise thermal imidization protocol for PCMA formation (Fig. S2). As illustrated in Fig. 1, the same P2C3 slurry was cast into a customized PTFE mold (Fig. S1(c and d)). The AH was then inserted and pressed into the slurry to achieve full infiltration of the cell volume prior to freezing. For PCMAC fabrication, the infiltrated slurry was likewise frozen in liquid nitrogen and freeze-dried using the same programmed schedule described in Section 2.2, followed by the same stepwise thermal imidization treatment.

2.4. Characterization

The morphology of the aerogels was observed by scanning electron microscope (SEM SU-5000, Hitachi, Japan) at an accelerated voltage of 20 kV. A thermogravimetric analyzer (TGA, Mettler Toledo, Switzerland) was employed to investigate the thermal stability of samples under an air atmosphere, with a heating rate of 10 °C/min from 25 °C to 800 °C. The functional groups of PI/CNT aerogels were observed by using a Fourier transform infrared spectroscopy (FTIR, Spectrum Two, PerkinElmer, UK). The relative complex permittivity (ε_r) and permeability (μ_r) in the frequency range of 2–18 GHz were measured using a vector network analyzer (E5071C, Agilent, USA) by the coaxial method. For coaxial measurements, molten paraffin was introduced into the PI/CNT aerogels at 100 °C to reinforce the fragile aerogel skeleton during coaxial-ring preparation. Paraffin was used as a low-loss, wave-transparent supporting medium to reduce damage

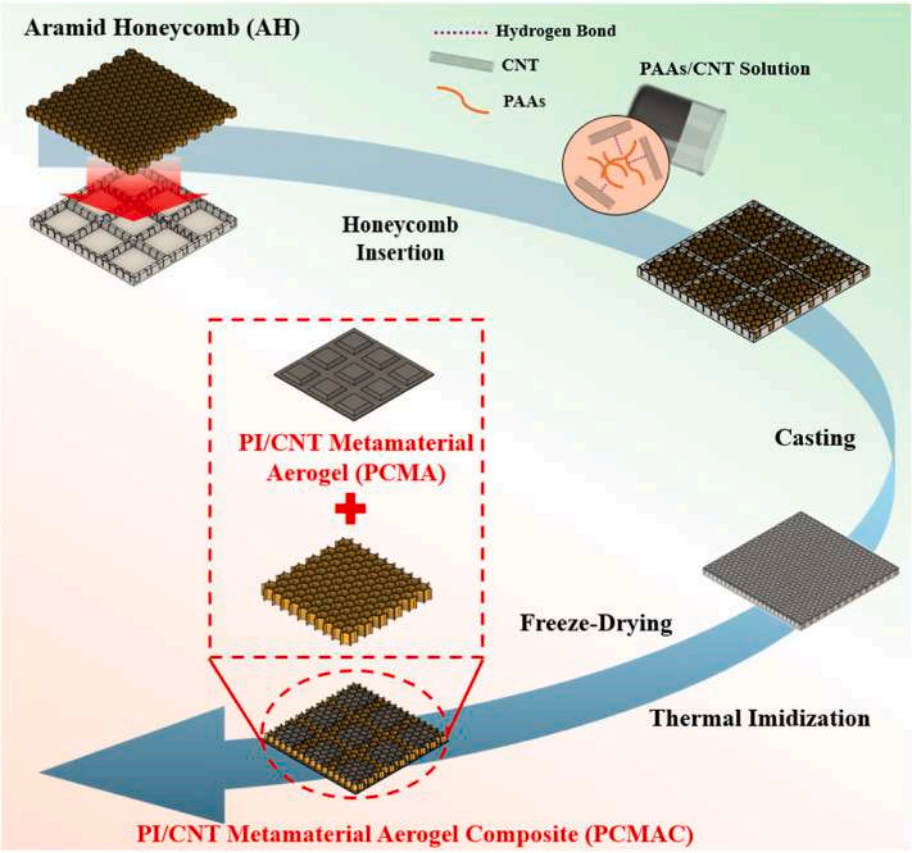

Fig. 1. The fabrication process flowchart of PI/CNT metamaterial aerogel composite (PCMAC).

during cutting. After cooling and solidification, the aerogel/paraffin composites were cut into coaxial rings with an outer diameter of 7 mm and an inner diameter of 3.02 mm. The mass ratio of aerogel to paraffin in the prepared coaxial specimens was approximately 7:93. All PI/CNT aerogel formulations were prepared using the same paraffin-infiltration procedure before coaxial testing. The reflection loss (RL) values of samples were calculated by the transmission line theory. The arc method (the same vector network analyzer as above) was applied to measure the RL of 200 mm × 200 mm samples in the frequency range of 2–18 GHz. For the free-space arch measurement, the specimen was prepared as an integral 3 × 3 unit-cell panel using the customized PTFE mold described in Fig. S1, rather than by post-fabrication splicing of smaller pieces. Therefore, no internal splicing gap was present within the tested area. For the metamaterial aerogels and their counterparts, measurements were conducted at incident angles of 5°, 15°, 30°, and 45° to evaluate the angular stability of microwave absorption. The measured electromagnetic parameters were imported into CST Microwave Studio 2023 for simulation. A genetic algorithm was coupled with CST to optimize the structural dimensions for maximum EAB within 2–18 GHz. The simulated RL was calculated using the finite integral method. For mechanical characterization, quasi-static three-point bending tests were performed according to GB/T1456-2021 using a universal mechanical tester (TY8000-A), with a loading rate of 2 mm/min and a support span of 160 mm. Compression tests were conducted using an electronic universal testing machine (C44-104, MTS) at a compression rate of 5 mm/min on 60 × 60 × 10 mm specimens.

3. Results and discussion

3.1. Fundamental properties of PI/CNT aerogels

To identify the most suitable PI/CNT aerogel composition for subsequent metamaterial construction, the fundamental properties of the three prepared formulations were systematically examined. Fig. 2 (a–c) shows the cross-sectional morphologies of P3C2, P1C1, and P2C3 at the cellular-network scale. All three samples exhibit interconnected porous frameworks. The enlarged images in Fig. 2(a1–c1) further show the local pore-wall morphology of the corresponding aerogel skeletons. P3C2 presents continuous sheet-like pore walls with comparatively smooth local surfaces. In P1C1, the pore-wall surface becomes more textured, and isolated CNT-like fibrous features can be observed along the folded wall regions. In P2C3, fibrous features are more frequently observed on the pore-wall surface and around skeletal junctions. The higher-magnification images in Fig. 2(a2–c2) provide a closer view of these local surface features, showing the transition from comparatively smooth pore-wall surfaces in P3C2 to fiber-containing pore-wall surfaces in P1C1 and P2C3.

The thermal processing window and chemical conversion behavior were further examined by TGA and FTIR. As shown in Fig. 3(a), both the neat PI aerogel and the PI/CNT aerogel retain more than 90 wt% of their initial mass up to approximately 500 °C in air. The aramid honeycomb begins to show noticeable mass loss near 420 °C. Since the maximum temperature used for stepwise thermal imidization is 250 °C, the selected thermal schedule remains below the apparent mass-loss region of all constituents and is therefore compatible with both the aerogel skeleton and the honeycomb reinforcement.

As shown in Fig. 3(b), the FTIR spectra of the neat PI and PI/CNT aerogels exhibit characteristic imide absorption bands, including asymmetric and symmetric C═O stretching near 1776 and 1720 cm^{-1}, C–N stretching near 1375 cm^{-1}, and imide ring deformation near 725 cm^{-1}. The amide-related C═O stretching band near 1660 cm^{-1}, characteristic of the poly(amic acid) precursor, is not resolved in either spectrum. This result indicates that the precursor has been substantially converted into the imide structure within the sensitivity of the FTIR

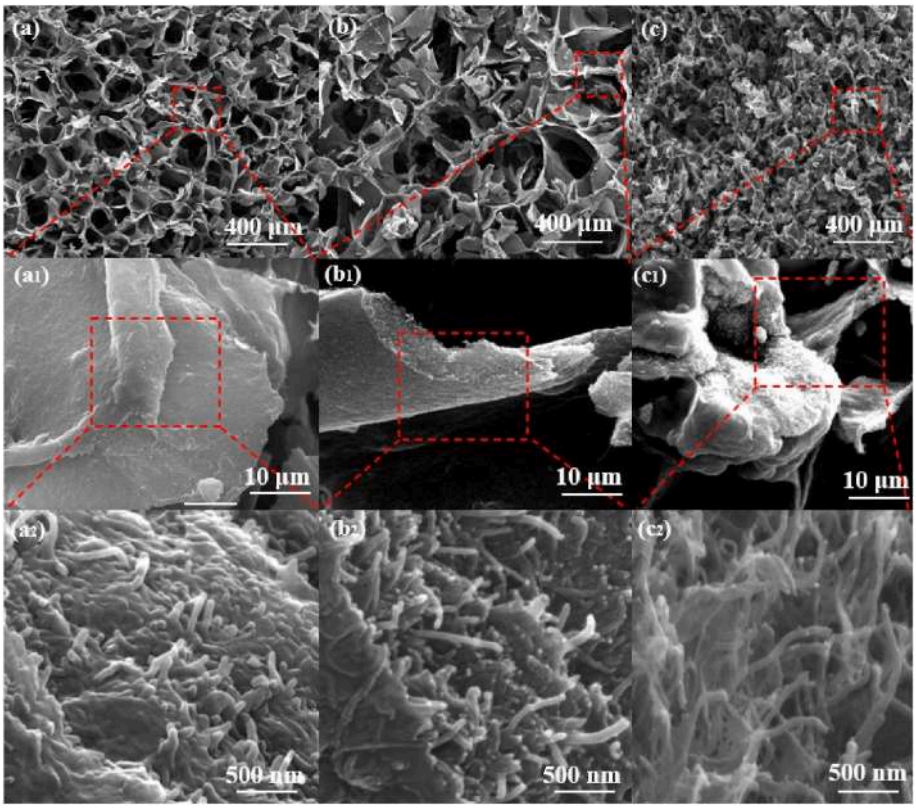

Fig. 2. SEM images of PI/CNT aerogels with different PI/CNT mass ratios. (a to c) Cross-sectional cellular morphologies of P3C2, P1C1, and P2C3, respectively. (a1 to c1) Enlarged views of selected pore-wall regions. (a2 to c2) Higher-magnification images of local pore-wall surface features.

measurement. The close spectral similarity between the neat PI and PI/CNT aerogels further indicates that CNT incorporation does not noticeably alter the imidization chemistry of the PI backbone [42]. Taken together, the TGA and FTIR results indicate that the thermal schedule is sufficient to achieve substantial imidization while remaining thermally compatible with the subsequent honeycomb-integrated fabrication process. The high residual mass retained by the PI and PI/CNT aerogels up to approximately 500 °C further confirms the thermal stability of the imidized aerogel framework under the present processing conditions.

The complex permittivity ($\varepsilon r = \varepsilon' - j\varepsilon''$) and complex permeability ($\mu r = \mu' - j\mu''$) were used to evaluate the electromagnetic response of the PI/CNT aerogels. As shown in Fig. S3, μ' remains close to 1 and μ'' remains close to 0 over 2–18 GHz, confirming that the present PI/CNT aerogels are dominated by dielectric loss. Therefore, the following analysis focuses on the complex permittivity. The complex permittivity spectra (Fig. 3(c–e)) provide the basis for selecting the matrix composition used in the subsequent metamaterial design. P2C3 exhibits the highest ε' over 2–15 GHz, indicating stronger polarization storage associated with the higher CNT fraction and the resulting PI/CNT interfacial structure [43–45]. Between 15 and 18 GHz, ε' decreases markedly, while ε'' shows a pronounced peak near 14 GHz (reaching ~8), which is characteristic of a Debye-type relaxation process [46,47]. The corresponding loss tangent of P2C3 peaks at approximately 1.3 at 16 GHz, exceeding those of P3C2 and P1C1, which remain below 0.4 throughout the measured band. This elevated dielectric loss is attributed to the combined contribution of CNT-induced conductive dissipation and interfacial polarization at PI–CNT boundaries [41,48]. Together with its higher ε' and ε'' over most of the measured band, P2C3 was selected as the base composition for subsequent metamaterial optimization and composite fabrication.

3.2. Structural size optimization of PCMA for electromagnetic performance based on GA

Metamaterial absorbers are commonly optimized by varying one geometric parameter at a time while keeping the other parameters fixed [25,49]. Such decoupled sweeps are insufficient for the present PI/CNT metamaterial aerogel because its broadband response is governed by several coupled geometric factors, including the front-surface filling fraction, the tapering ratio, the substrate thickness, and the available lossy volume. Therefore, a genetic-algorithm-assisted full-wave simulation strategy was adopted to search the coupled structural design space and identify a broadband absorber under a fixed total thickness of 10 mm.

As shown in Fig. 4(a), the parametric unit-cell model was governed by four continuous variables: base side length L1, substrate thickness t, and two length ratios $R_1 = L_2/L_1$ and $R_2 = L_3/L_2$, with the total height fixed at $H = h + t = 10$ mm. When $R_1 = R_2 = 1$, the unit cell reduces to a uniform slab. Decreasing R_1 and R_2 generates a family of stepped geometries, including a square stepped structure, a frustum, and finally a pyramid-like structure as the upper side length is strongly reduced. Thus, the slab, square, pyramid, and optimized PCMA used in Fig. 5 were derived from the same parametric design framework.

The initial population was generated by Latin Hypercube Sampling, and the population was evolved through selection, crossover, and mutation operators while geometrically invalid candidates were excluded (Fig. 4(b)). The primary objective is to maximize the EAB across the full spectrum (2–18 GHz). The fitness function F(X) is defined as the integral of the valid absorption frequency range as follows:

$$F(X) = \int_{fmin}^{f_{max}} \delta(f, X)df \quad (1)$$

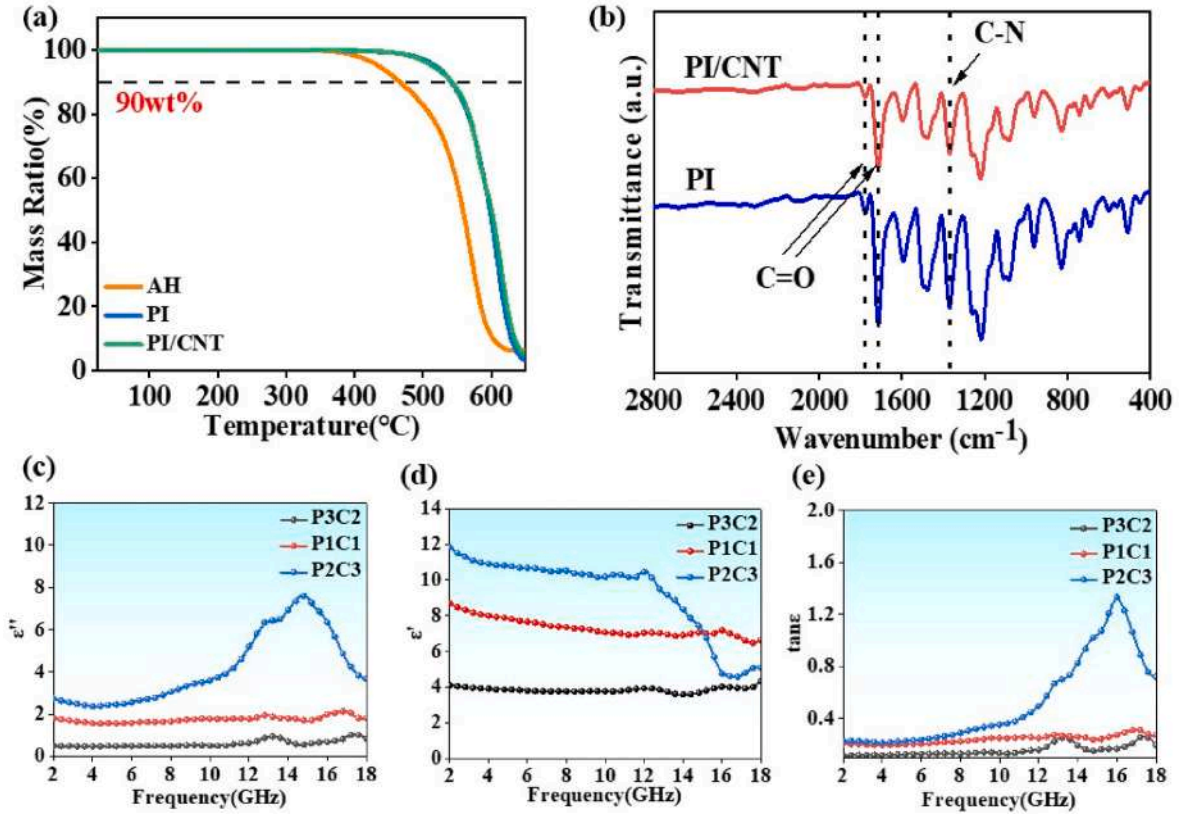

Fig. 3. Thermal, chemical, and dielectric characterization of PI/CNT aerogels. (a) TGA curves of aramid paper, neat PI aerogel, and PI/CNT aerogel under air atmosphere. The dashed line marks 90 wt% residual mass. (b) FTIR spectra of neat PI and PI/CNT aerogels. (c to e) Frequency-dependent ε', ε'', and tanδ of P3C2, P1C1, and P2C3 measured over 2 to 18 GHz by the coaxial method.

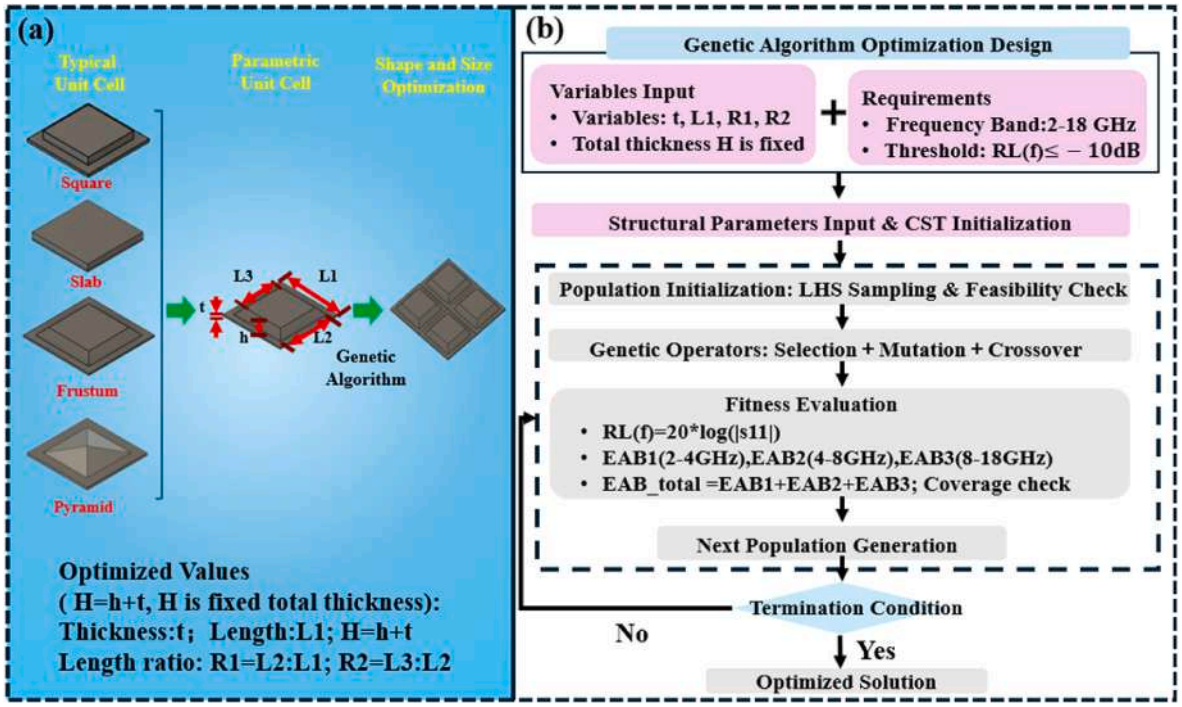

Fig. 4. Parametric unit-cell model and GA optimization. (a) Parametric unit-cell model with four continuous design variables (base side length L1, substrate thickness t, and two geometric ratios $R_1 = L_2/L_1$ and $R_2 = L_3/L_2$) under a fixed total thickness $H = h + t = 10$ mm. The model spans a continuous family of shapes from uniform slab (R1 = R2 = 1) through square, frustum to pyramid (R1, R2 → 0). The optimized values are listed below the model. (b) GA optimization workflow.

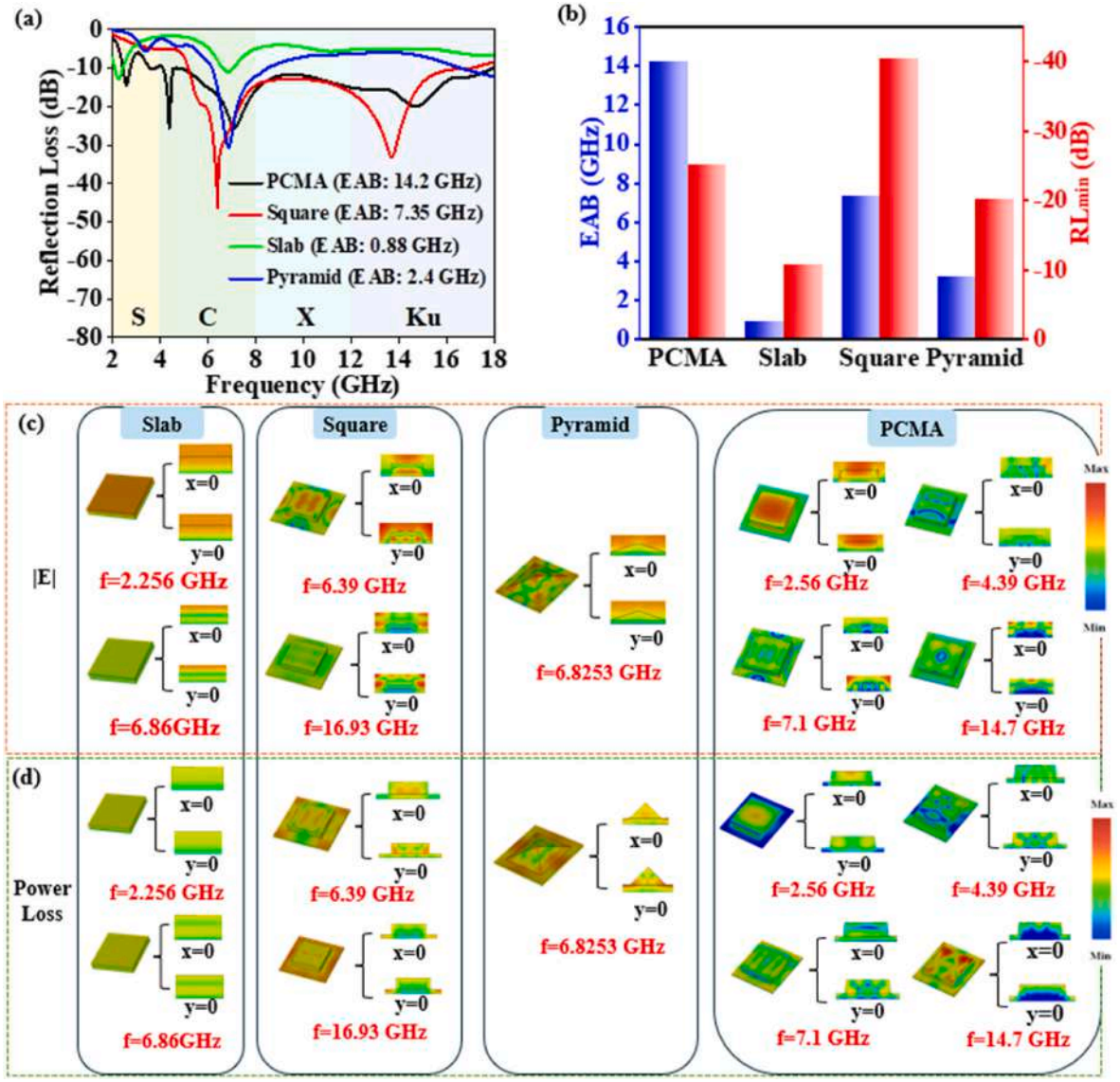

Fig. 5. Simulated electromagnetic performance comparison of GA-optimized structural designs. (a) Simulated reflection loss (RL) spectra of the slab, square, pyramid, and optimized PCMA frustum over 2–18 GHz. (b) EAB and RLmin of the four structural configurations. (c) Simulated electric-field magnitude (|E|) distributions of the slab, square, pyramid, and PCMA at representative frequencies, shown in x = 0 and y = 0 cross-sections. (d) Corresponding power loss density distributions, illustrating the progression from surface-confined dissipation (slab) to volumetric broadband attenuation (PCMA).

$$\delta(f,X)=\begin{cases}1, \text{if } RL(f,X)\ll -10dB\\ 0, \text{otherwise}\end{cases} \quad (2)$$

where $RL(f,X)=20*\log|S_{11}(f,X)|$ represents the simulated reflection loss at frequency f, $\delta(f,X)$ represents a logical gate that equals 1 when the 90% absorption criterion is satisfied and 0 otherwise. To ensure engineering feasibility, the total thickness (H) was imposed as a rigid constraint, and the design variables were bounded within manufacturable limits.

Because the optimization target was broadband EAB, the selected structure was determined by absorption-band coverage rather than by the deepest RL_{min}. The GA converged to a frustum-type PCMA with L_1 = 66.37 mm, L_2 = 48.45 mm, L_3 = 45.54 mm, h = 7.25 mm, and t = 2.75 mm. This geometry lies between the limiting slab and pyramid cases, providing a compromise between front-surface impedance transition and internal lossy volume. L_1, t, R_1, and R_2 jointly define the entrance impedance transition, effective dielectric loading, geometric transition, and available lossy volume. The resulting frustum geometry therefore represents a coupled optimum under the EAB objective, fixed-thickness constraint, and manufacturability considerations.

The optimized PCMA was then compared with three representative geometries from the same framework, namely the uniform slab, square stepped structure, and pyramid-like structure. The electromagnetic performance of the optimized PCMA and the three representative comparison geometries is shown in Fig. 5(a and b). The monolithic slab exhibits an EAB of only 1.89 GHz because the planar air–aerogel interface causes severe impedance mismatch and limits wave penetration [50]. The square stepped structure improves the EAB to approximately 7.35 GHz owing to its larger cross-sectional area and increased lossy volume, but the abrupt orthogonal boundary at the top surface still induces interfacial reflection. The pyramid configuration provides a smoother impedance transition from free space, but its sharp apex and progressively reduced cross-section limit the available lossy volume, resulting in an EAB of only 2.4 GHz. By comparison, the optimized PCMA achieves the widest simulated EAB because it balances gradual impedance transition with sufficient internal lossy volume under the fixed 10 mm thickness constraint.

The field and power-loss distributions in Fig. 5(c and d) further

support the structural comparison. In the slab, the electric field and power loss are mainly confined near the incident surface, indicating limited wave penetration caused by the abrupt planar interface. In the square stepped structure, the field extends further into the absorber, but pronounced field concentration remains near the orthogonal top boundaries. In the pyramid, the tapered profile improves the entrance transition, while the reduced cross-section confines the loss region to a narrower central volume. For the optimized PCMA, field penetration and power-loss distribution are more spatially extended within the frustum body. At 2.56 GHz, the electric field penetrates through a substantial portion of the frustum. At 4.39 and 7.10 GHz, enhanced fields appear along the lateral transition regions while interior field penetration is retained. At 14.7 GHz, the loss region becomes more localized near the upper transition regions and corners. These frequency-dependent distributions indicate that the broadband response originates from the combined effects of impedance transition, accessible lossy volume, and local field redistribution within the fixed 10 mm thickness.

3.3. Electromagnetic simulation of honeycomb-reinforced PCMAC structures

Based on the GA-optimized PCMA geometry, honeycomb-reinforced PCMAC models were constructed to evaluate the influence of commercial AH cell size on broadband absorption. Three AH cell sizes, 3.2, 6.4, and 9.6 mm, were selected as practical commercial specifications, representing relatively dense, intermediate, and sparse wall distributions within the same metamaterial geometry. Since the optimization target was EAB over 2–18 GHz, the cell-size effect was evaluated by combining local absorption-peak evolution with broadband impedance-matched bandwidth. In this broadband evaluation, the wavelength associated with one absorption peak is treated as a local descriptor, while the overall cell-size dependence is assessed from the full reflection-loss and impedance responses.

As shown in Fig. 6(a and b), changing the honeycomb cell size affects the reflection-loss peak position, peak depth, and EAB in a frequency-dependent manner. Near 8 GHz, the local absorption peak becomes deeper as the cell size decreases from 9.6 to 3.2 mm, indicating stronger frequency-selective attenuation associated with the increased wall density in this region. This local trend does not extend over the full 2–18 GHz band. Accordingly, no monotonic relationship is observed between honeycomb cell size and the characteristic RL_{min} peak over the 2–18 GHz range. PCMAC-3.2 exhibits the deepest RL_{min} within a limited frequency range, whereas PCMAC-9.6 provides the widest EAB among the honeycomb-integrated structures. The following analysis therefore focuses on broadband impedance matching [51], field/loss

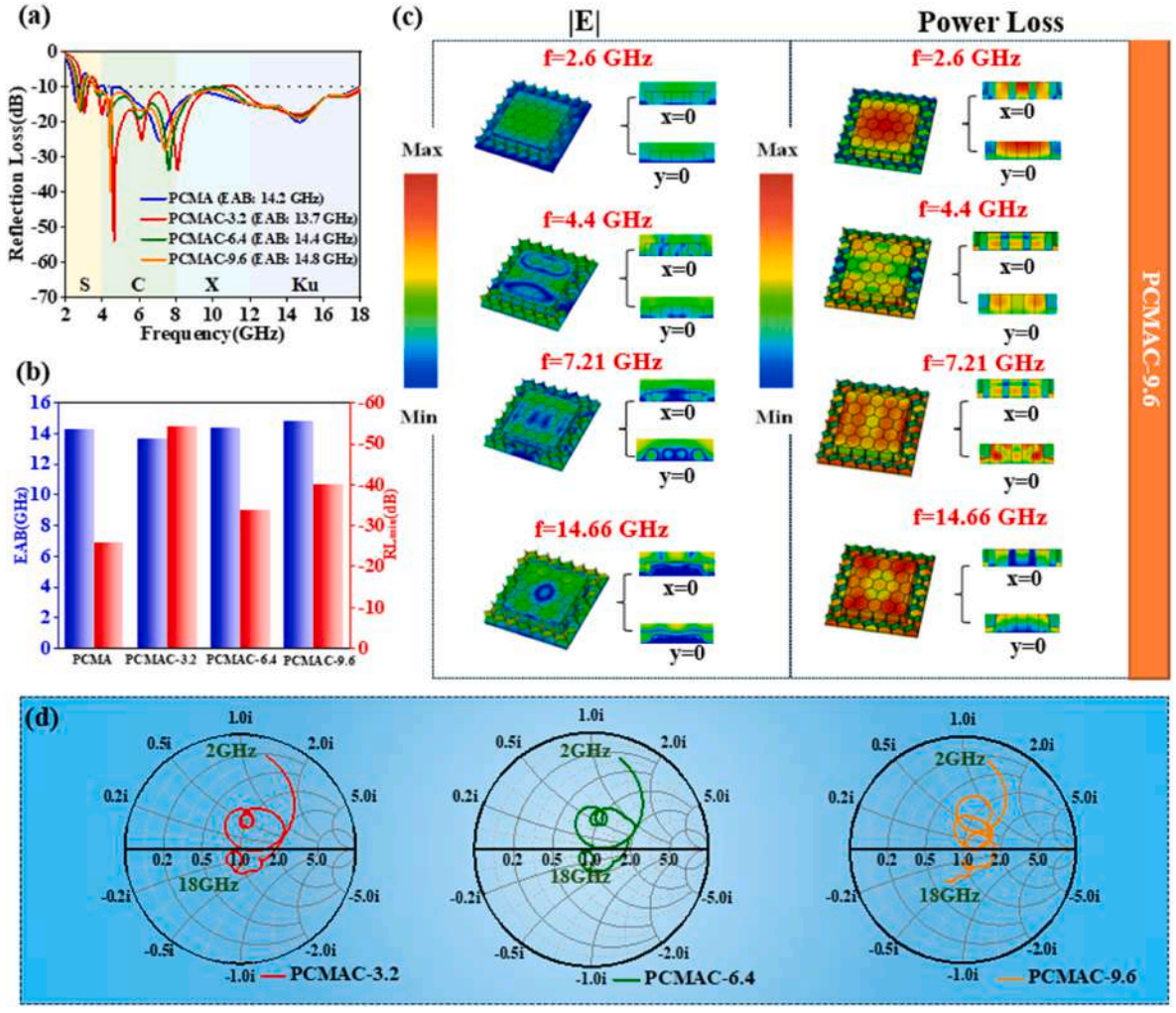

Fig. 6. Simulated electromagnetic performance of PCMA and PCMAC with different honeycomb cell sizes. (a) Simulated RL spectra of PCMA, PCMAC-3.2, PCMAC-6.4, and PCMAC-9.6 over 2–18 GHz. (b) Comparison of EAB and RLmin for the four configurations. (c) Electric-field magnitude and power-loss density distributions of PCMAC-9.6 at representative absorption frequencies, shown in x = 0 and y = 0 cross-sections. (d) Smith charts of PCMA, PCMAC-3.2, PCMAC-6.4, and PCMAC-9.6 over 2–18 GHz.

redistribution, and preservation of the impedance response of the GA-optimized PCMA geometry.

The microwave attenuation of PCMAC involves both microscopic dielectric-loss pathways and macroscopic impedance regulation. In the P2C3 aerogel, CNT-induced conductive dissipation and PI/CNT interfacial polarization provide the primary dielectric-loss contribution [52–54]. Honeycomb integration further introduces AH/aerogel contact regions and aramid-fiber/resin interfaces within the honeycomb walls, which may serve as auxiliary polarization sites and local field-redistribution regions. The broadband absorption of PCMAC is therefore associated with dielectric attenuation in the aerogel phase, interfacial effects introduced by the honeycomb skeleton, and the impedance-transition pathway established by the GA-optimized frustum geometry.

Decreasing the cell size increases the number of honeycomb walls and AH/aerogel contact regions within the same projected area. The increased wall density in the smaller-cell configurations can enhance local frequency-selective attenuation, as reflected by the local peak evolution in Fig. 6(a and b). Over the broadband range, however, it also modifies the continuity of the designed impedance-transition pathway. By comparison, PCMAC-9.6 better preserves the impedance trajectory and field-penetration characteristics of the optimized PCMA, which is consistent with its wider impedance-matched bandwidth.

Fig. 6(c) further shows the electric-field and power-loss density distributions of PCMAC-9.6 at representative absorption frequencies. PCMAC-9.6 maintains appreciable field penetration into the frustum body and forms spatially distributed power-loss regions. Additional field and power-loss maps for PCMAC-3.2 and PCMAC-6.4 are provided in Fig. S5. Compared with PCMAC-9.6, the smaller-cell configurations show less spatially continuous high-frequency loss regions within the frustum body, indicating that the increased wall density modifies the internal field distribution of the optimized metamaterial geometry. These field maps are consistent with the wider EAB of PCMAC-9.6 and support the view that the 9.6 mm honeycomb better preserves the field-penetration and volumetric-dissipation characteristics of the GA-optimized PCMA.

This field-distribution result is consistent with the Smith-chart trajectories in Fig. 6(d) and the normalized input impedance spectra in

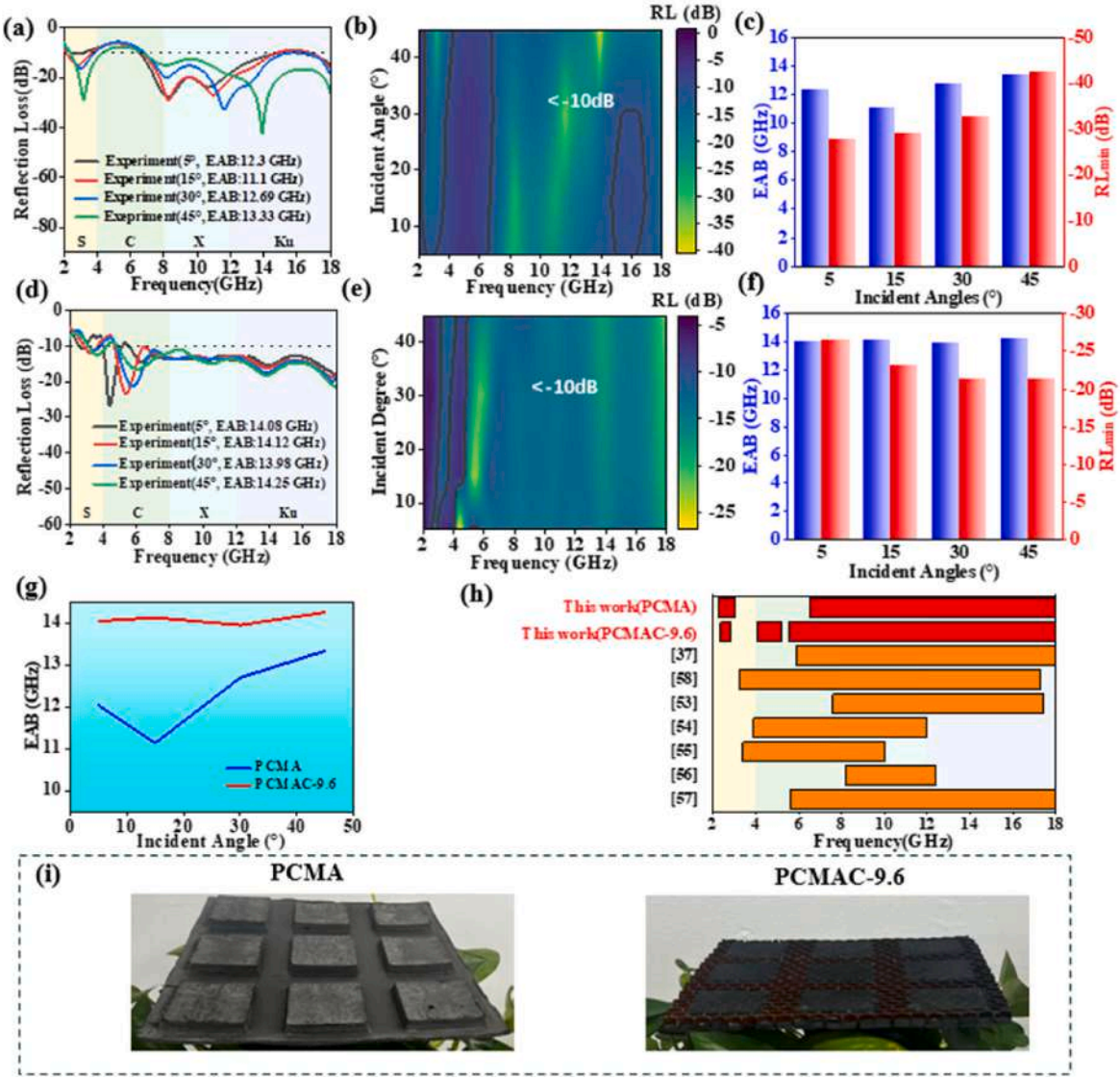

Fig. 7. Experimental electromagnetic performance and comparison of PCMA and PCMAC-9.6. (a) Measured RL spectra of PCMA at incident angles of 5°, 15°, 30°, and 45°. (b) RL contour map of PCMA versus frequency and incident angle. (c) EAB and RL_{min} of PCMA at each angle. (d) Measured RL spectra of PCMAC-9.6 at the same angles, compared with simulation. (e) RL contour map of PCMAC-9.6. (f) EAB and RL_{min} of PCMAC-9.6 at each angle. (g) Experimental EAB of PCMA and PCMAC-9.6 as a function of incident angle, illustrating the angular stability imparted by the honeycomb. (h) Comparison of EAB with reported aerogel-based and metamaterial absorbers at comparable thickness (≤10 mm). (i) Photographs of the PCMA sample and the PCMAC-9.6 sample.

Fig. S4. PCMAC-9.6 follows the PCMA trajectory most closely and forms the most compact trajectory near the chart-center region, while maintaining Re(Z_{in}/Z_0) closer to unity and Im(Z_{in}/Z_0) closer to zero over a broader frequency interval [55]. By comparison, PCMAC-3.2 and PCMAC-6.4 show larger low-frequency impedance deviations, consistent with their narrower EABs and less continuous field/loss distributions. Among the simulated commercial cell sizes, the 9.6 mm honeycomb therefore provides the most favorable balance between preserving the GA-optimized impedance response and maintaining field penetration into the frustum body. Accordingly, PCMAC-9.6 was selected for experimental fabrication and characterization.

3.4. Experimental electromagnetic performance of PCMA and PCMAC

The electromagnetic performance of the fabricated samples was measured using a free-space arch system in an anechoic chamber (Fig. S6). Fig. 7(a) presents the measured RL spectra of PCMA. The contour map (Fig. 7(b)) shows that the absorption band narrows and shifts with increasing incident angle. Quantitatively, the experimental EAB varies between approximately 11.5 and 13.8 GHz depending on the incident angle (Fig. 7(c)). Compared with the simulated EAB of the PCMA geometry, the measured PCMA shows a reduced absorption bandwidth and weaker angular stability.

This deviation between the simulated and measured PCMA responses is mainly associated with the measurement condition and processing-induced geometric deformation. The simulation was conducted using the optimized geometry under normal incidence, whereas the experimental free-space arch measurement started from 5° incidence, which can contribute to spectral deviation. In addition, the free-standing PCMA panel underwent shrinkage during freeze-drying and thermal imidization. For the present stepped-frustum geometry, through-thickness contraction of the thin base layer, local bending, edge rounding, and dimensional contraction of the frustum body can alter the designed impedance-transition pathway and affect the measured absorption response. The dimensional measurements in Fig. S8 and Table S2 show pronounced shrinkage and profile distortion in the free-standing PCMA panel, providing direct evidence that geometric deformation is a major observable contributor to the discrepancy between simulation and experiment.

To quantify the geometric deformation, the key dimensions of the fabricated PCMA and PCMAC-9.6 panels were measured at three positions on each panel using a stainless-steel ruler with 0.5 mm graduation (Table S2; Fig. S8). The free-standing PCMA panel shows pronounced contraction: L decreases from 199.1 mm to 188.8 ± 0.5 mm, L_3 from 45.5 mm to 40.8 ± 0.5 mm, H from 10.0 mm to 8.6 ± 0.5 mm, and t from 2.75 mm to 1.8 ± 0.5 mm.

By comparison, PCMAC-9.6 shows much smaller dimensional changes after fabrication. The measured dimensions are L = 199.1 ± 0.5 mm, L_3 = 45.1 ± 0.5 mm, H = 9.9 ± 0.5 mm, and t = 2.7 ± 0.5 mm, which are close to the corresponding design values of 199.1, 45.5, 10.0, and 2.75 mm. These results indicate that the AH skeleton effectively constrains processing-induced shrinkage, improves panel flatness, and helps preserve the designed frustum profile during fabrication. The closer agreement between the measured and simulated responses of PCMAC-9.6 is therefore mainly associated with the improved geometric preservation introduced by the honeycomb skeleton.

The role of the macrostructural design was further examined using control samples measured under the same arch conditions. The 10 mm-thick uniform P2C3 monolithic slab (Fig. S7(a)) exhibits an EAB of approximately 1.35 GHz at 5° incidence, which is much narrower than that of PCMA at the same angle. This comparison indicates that the EAB improvement achieved by PCMA is mainly associated with the GA-optimized macrostructural geometry. When the honeycomb cells are uniformly filled with P2C3 (Fig. S7(b)), the EAB broadens compared with the uniform P2C3 slab, indicating that the honeycomb skeleton introduces additional impedance modulation. PCMAC-9.6 further provides a wider absorption band than the uniformly filled honeycomb structure, indicating that the GA-optimized metamaterial geometry plays the primary role in broadband absorption, while the AH skeleton contributes through complementary impedance modulation and geometric stabilization.

Fig. 7(h) benchmarks the measured EAB of PCMAC-9.6 against representative aerogel-based and metamaterial absorbers reported in the literature [35,56–61], with detailed parameters summarized in Table S3. Among samples with comparable thickness (≤10 mm), PCMAC-9.6 achieves an EAB of 14.01 GHz, exceeding the rGO/BC aerogel-filled honeycomb (12.1 GHz at 10 mm) [35], the CF/PIA6 metamaterial (12.4 GHz at 8 mm) [60], and the 3D-printed ABS/Carbon and CB/PP metamaterials (8.1 and 6.6 GHz at 9.37 and 10 mm, respectively) [57,58]. Monolithic aerogel absorbers such as PI/PPC@CNC [56] and CNTs/cellulose@TPU [59] exhibit EABs of 9.8 and 4.2 GHz at thicknesses of 7.8 and 7.66 mm, respectively, without the same macrostructural impedance-gradient design used in the present PCMAC structure. The graphene/SiO_2 aerogel [61] attains a comparable EAB of 14.04 GHz but requires a thickness of 20 mm, twice that of the present design. The combination of GA-optimized metamaterial geometry and honeycomb reinforcement indicates that PCMAC-9.6 achieves a comparatively wide EAB among the representative aerogel-based and metamaterial absorbers surveyed here under a 10 mm thickness constraint.

3.5. Mechanical performance of the PCMAC and PCMA

For practical aerospace applications, mechanical robustness is equally important. To clarify the mechanical contribution of the integrated architecture, comparative tests were conducted on the empty aramid honeycomb (AH), pure PCMA, and PCMAC-9.6 under both out-of-plane compression and three-point bending. Fig. 8(a and b) presents the compression test setup and representative stress–strain curves. The empty AH exhibits a linear elastic rise followed by a sharp stress drop at approximately 3.2 MPa, corresponding to plastic buckling of the thin aramid cell walls, after which the stress enters a densification plateau. The pure PCMA collapses earlier and reaches approximately 2.4–2.5 MPa, reflecting the limited compressive stability of the free-standing aerogel architecture. By comparison, PCMAC-9.6 reaches a compressive strength of 4.3 MPa, corresponding to a 34% increase relative to AH and an approximately 70–80% increase relative to pure PCMA. This higher compressive strength indicates that the honeycomb-supported configuration provides a more stable load-bearing framework than the free-standing PCMA under out-of-plane compression.

Three-point bending results are shown in Fig. 8(c and d). The empty AH exhibits a nominal flexural strength of approximately 0.45 MPa, whereas the pure PCMA shows lower bending resistance, with a nominal flexural strength of approximately 0.17–0.20 MPa. PCMAC-9.6 reaches approximately 0.80 MPa, which is 78% higher than that of AH and more than four times that of pure PCMA. Together with the compression results, the bending data show that PCMAC-9.6 provides the highest load-bearing response among the three tested configurations. This improvement is associated with the integrated honeycomb-supported aerogel architecture, in which the honeycomb skeleton provides structural constraint and the filled aerogel phase helps maintain structural continuity under loading.

To assess repeatability, three parallel specimens were tested for each condition. The individual results are summarized in Fig. 8(e), and the limited data scatter is consistent with the observed ranking among the three configurations. The bending failure process of PCMAC-9.6 is captured in Fig. 8(f). In stage I, the composite deforms elastically. In stage II, progressive yielding develops in the honeycomb core, while the filled aerogel phase remains retained within the honeycomb cells and helps maintain structural continuity during bending. Final failure (stage III) occurs via core shear fracture near the loading nose. The specimen remains integral after failure, suggesting that the honeycomb-supported

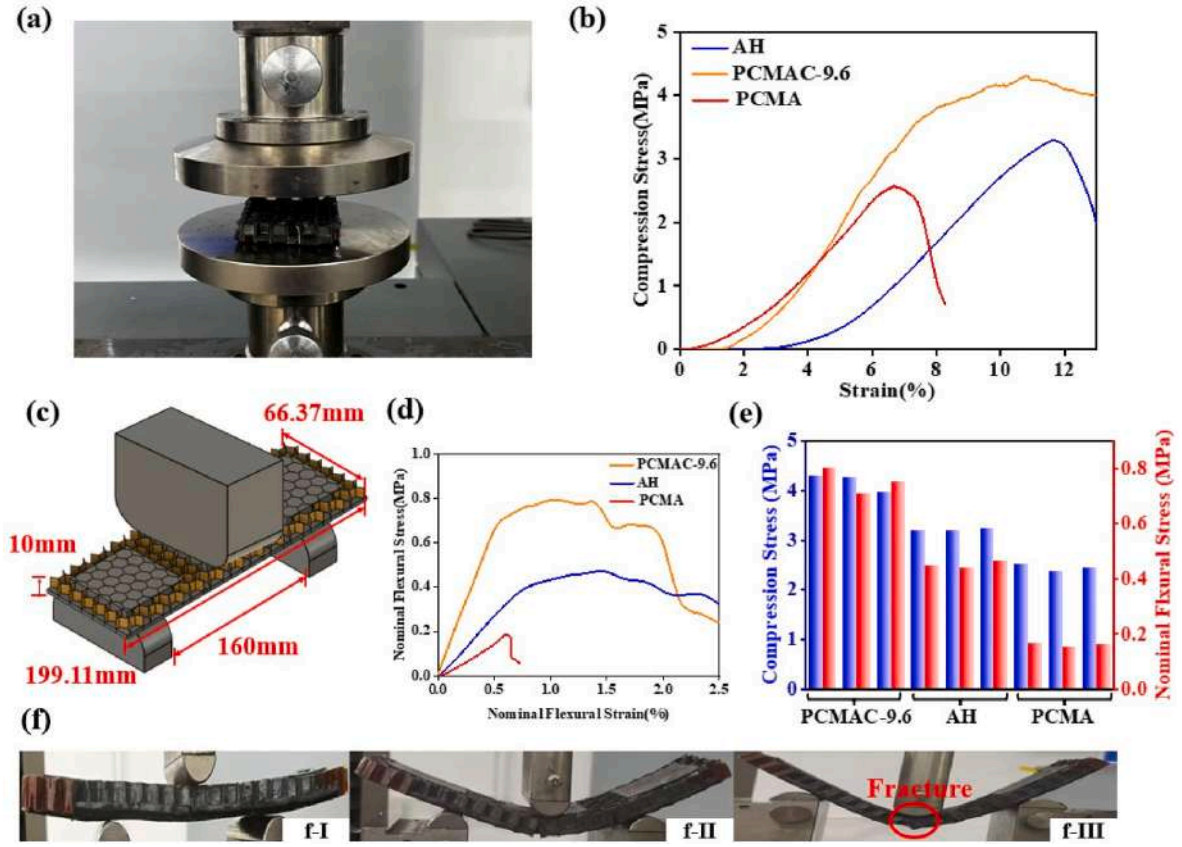

Fig. 8. Mechanical performance of the empty aramid honeycomb (AH), pure PCMA, and PCMAC-9.6 under out-of-plane compression and three-point bending. (a) Photograph of the out-of-plane compression test setup. (b) Representative compressive stress–strain curves of AH, pure PCMA, and PCMAC-9.6. (c) Schematic of the three-point bending test configuration (span = 160 mm, loading rate = 2 mm/min). (d) Representative nominal flexural stress–strain curves of AH, pure PCMA, and PCMAC-9.6. (e) Compressive yield strength and nominal flexural strength of AH, pure PCMA, and PCMAC-9.6 measured from three parallel specimens for each condition; error bars indicate ±1 standard deviation. (f) Photographs of the PCMAC-9.6 bending failure process: (f-I) elastic deformation, (f-II) progressive core yielding while structural continuity is maintained, and (f-III) final core shear fracture near the loading nose.

configuration helps maintain structural continuity during bending.

4. Conclusions

This study presents a honeycomb-reinforced metamaterial aerogel composite (PCMAC) designed to improve geometric stability, broadband microwave absorption, and mechanical load-bearing capacity. A parametric unit-cell model spanning slab-to-pyramid geometries was coupled with a genetic algorithm to optimize the absorber geometry under a fixed thickness of 10 mm. The optimizer converged on a frustum configuration (L1 = 66.37 mm, R1 = 0.73, R2 = 0.94, t = 2.75 mm), which balances entrance impedance transition, accessible lossy volume, and local field redistribution. Compared with the uniform slab, the optimized frustum broadens the simulated EAB from 1.89 GHz to 14.2 GHz.

The aramid honeycomb skeleton reduces processing-induced geometric deformation and helps preserve the GA-optimized frustum profile during freeze-drying and thermal imidization. Among the investigated commercial cell sizes, PCMAC-9.6 shows the closest impedance trajectory to PCMA and maintains more continuous field penetration and power-loss distribution within the frustum body, giving the widest simulated EAB among the honeycomb-reinforced structures. The fabricated PCMAC-9.6 achieves an experimental EAB of 13.9–14.3 GHz over 2–18 GHz and maintains stable absorption from 5° to 45° incidence.

Mechanically, PCMAC-9.6 reaches compressive and nominal flexural strengths of 4.30 MPa and 0.80 MPa, respectively. These values are 34% and 78% higher than those of the empty honeycomb, and are also approximately 70–80% and more than fourfold higher than those of pure PCMA, respectively. The compression, bending, and failure-process observations indicate that the honeycomb-supported aerogel architecture improves specimen-level load-bearing capacity while maintaining structural continuity during deformation. These results demonstrate a practical route for integrating gradient metamaterial aerogels with aramid honeycomb frameworks to obtain lightweight multifunctional absorbers with combined electromagnetic and mechanical performance.

CRediT authorship contribution statement

Zibo Li: Writing – review & editing, Validation, Resources, Project administration, Methodology. **Zhichun Zhang:** Writing – review & editing. **Anping Wang:** Writing – review & editing, Supervision, Resources, Project administration, Funding acquisition. **Yanju Liu:** Writing – review & editing, Supervision, Resources, Project administration, Funding acquisition. **Jinsong Leng:** Funding acquisition, Project administration, Resources, Supervision, Writing – review & editing.

Declaration of competing interest

The authors declare that they have no known competing financial interests or personal relationships that could have appeared to influence the work reported in this paper.

Acknowledgement

This research is supported by National Natural Science Foundation of China (Granted No. 92271206).

Appendix A. Supplementary data

Supplementary data to this article can be found online at https://doi.org/10.1016/j.compositesb.2026.113777.

Data availability

Data will be made available on request.

References

[1] Zhang X, Cheng J, Xiang Z, Cai L, Lu W. A hierarchical Co@mesoporous C/macroporous C sheet composite derived from bimetallic MOF and Oroxylum indicum for enhanced microwave absorption. Carbon 2022;187:477–87. https://doi.org/10.1016/j.carbon.2021.11.044.

[2] Chang M, Li Q, Jia Z, Zhao W, Wu G. Tuning microwave absorption properties of Ti3C2Tx MXene-based materials: component optimization and structure modulation. J Mater Sci Technol 2023;148:150–70. https://doi.org/10.1016/j.jmst.2022.11.021.

[3] Wu L, Liu J, Liu X, Mou P, Lv H, Liu R, Wen J, Zhao J, Li J, Wang G. Microwave-absorbing foams with adjustable absorption frequency and structural coloration. Nano Lett 2024;24:3369–77. https://doi.org/10.1021/acs.nanolett.3c05006.

[4] Zhu X, Dong Y, Xiang Z, Cai L, Pan F, Zhang X, Shi Z, Lu W. Morphology-controllable synthesis of polyurethane-derived highly cross-linked 3D networks for multifunctional and efficient electromagnetic wave absorption. Carbon 2021;182:254–64. https://doi.org/10.1016/j.carbon.2021.06.028.

[5] Yan L, Wang J, Han X, Ren Y, Liu Q, Li F. Enhanced microwave absorption of Fe nanoflakes after coating with SiO2 nanoshell. Nanotechnology 2010;21:095708. https://doi.org/10.1088/0957-4484/21/9/095708.

[6] Liu L, Duan Y, Ma L, Liu S, Yu Z. Microwave absorption properties of a wave-absorbing coating employing carbonyl-iron powder and carbon black. Appl Surf Sci 2010;257:842–6. https://doi.org/10.1016/j.apsusc.2010.07.078.

[7] Yang Z, Luo F, Hu Y, Duan S, Zhu D, Zhou W. Dielectric and microwave absorption properties of TiO2/Al2O3 coatings and improved microwave absorption by FSS incorporation. J Alloys Compd 2016;678:527–32. https://doi.org/10.1016/j.jallcom.2016.04.031.

[8] Zhang X, Wang Z, Zhou G, Li J, Li C, Lin C, Xin X. Multifunctional metamaterials based on MXene composite aerogels for integrated load-bearing and multiphysics wave attenuation. Composites, Part B Eng 2026;309:113075. https://doi.org/10.1016/j.compositesb.2025.113075.

[9] Wang X, Yuan Y, Sun X, Qiang R, Xu Y, Ma Y, Zhang E, Li Y. Lightweight, flexible, and thermal insulating Carbon/SiO2@CNTs composite aerogel for high-efficiency microwave absorption. Small 2024;20:2311657. https://doi.org/10.1002/smll.202311657.

[10] Jin Y, Zhang J, Cao S, Xu J, Fan H, Tabassum Z, Chen K, Yang S. Heterointerfaced PAN/CNTs/Ni aerogel for heat insulation, sound and electromagnetic wave absorption. Compos Commun 2025;57:102427. https://doi.org/10.1016/j.coco.2025.102427.

[11] Cai Z, Yang H, Zhou H, Lin Y, Cheng Y, Yuan Q. Achieving efficient electromagnetic absorption in multifunctional carbon nanotube aerogels by manipulating radialized network structure. Chem Eng J 2024;498:155629. https://doi.org/10.1016/j.cej.2024.155629.

[12] Wu F, Hu P, Hu F, Liao Z, Cheng L. Multifunctional MXene/C aerogels for enhanced microwave absorption and thermal insulation. Nano-Micro Lett 2023;15:194. https://doi.org/10.1007/s40820-023-01158-7.

[13] Lin J, Liu J, Zhang K, Deng Y, Che W, Pang X, Zhang Q, Cai W, Zeng Z, Wu N. Ambient-pressure-dried aerogel amplifies interfacial polarization toward high-efficiency microwave absorption. Adv Funct Mater 2025:202520336. https://doi.org/10.1002/adfm.202520336.

[14] Cheng Y, Sun X, Yang S, Wang D, Liang L, Wang S, Ning Y, Yin W, Li Y. Multifunctional elastic rGO hybrid aerogels for microwave absorption, infrared stealth and heat insulation. Chem Eng J 2023;451:139376. https://doi.org/10.1016/j.cej.2022.139376.

[15] Zhang Y, Yang SH, Xin Y, Kang YF, Wang JX, Liang YP, He SA. Designing symmetric gradient honeycomb structures with carbon-coated iron-based composites for high-efficiency microwave absorption. Nano-Micro Lett 2024;16:234. https://doi.org/10.1007/s40820-024-01435-z.

[16] Ji B, Fan S, Kou S, Xia X, Deng J, Cheng L, Zhang L. Microwave absorption properties of multilayer impedance gradient absorber consisting of Ti3C2Tx MXene/polymer films. Carbon 2021;181:130–42. https://doi.org/10.1016/j.carbon.2021.05.018.

[17] Wang L, Yu X, Huang M, You W, Zeng Q, Zhang J, Liu X, Wang M, Che R. Orientation growth modulated magnetic-carbon microspheres toward broadband electromagnetic wave absorption. Carbon 2021;172:516–28. https://doi.org/10.1016/j.carbon.2020.09.050.

[18] Gai L, Chen Y, Wang Y, Zhang L, Liu X, Shui J. Engineering impedance-matched double-shells in hollow Co/carbon microspheres with gradient graphitization for high-efficiency electromagnetic wave absorption. J Adv Ceram 2025;14:9221212. https://doi.org/10.26599/JAC.2025.9221212.

[19] Pan J, Li X, Xia W, Qu H, Li J, Jiang C, Wang T, He J. Improvement of multiple attenuation and optimized impedance gradient for excellent multilayer microwave absorbers derived from two-dimensional metal–organic frameworks. Chem Eng J 2023;452:139601. https://doi.org/10.1016/j.cej.2022.139601.

[20] He L, Li X, Zhao Y, Zhong Z, Zhang J, Yang Y, Xi X. The multilayer structure design of magnetic-carbon composite for ultra-broadband microwave absorption via PSO algorithm. J Alloys Compd 2022;913:165088. https://doi.org/10.1016/j.jallcom.2022.165088.

[21] Li K, Liu Z, Wang Y, Zhang P, Lin Z, Fan S, Xin T, Du H, Luo Z, Wang C, Yang W, Yang J. Microwave absorption properties and multilayer absorber design of La2FexCo14-xB with easy cone anisotropy. J Alloys Compd 2025;1010:177561. https://doi.org/10.1016/j.jallcom.2024.177561.

[22] Zhang H, Cheng J, Liu K, Jiang S, Zhang J, Wang Q, Lan C, Jia H, Li Z. Electric-magnetic dual-gradient structure design of thin MXene/Fe3O4 films for absorption-dominated electromagnetic interference shielding. J Colloid Interface Sci 2025;678:950–8. https://doi.org/10.1016/j.jcis.2024.08.216.

[23] Shin SC, Hong M, Lee SE. Double-layered radar absorbing MWCNT/PDMS composites optimized by genetic algorithm using complex permittivity as a continuous variable. Compos Part A Appl Sci Manuf 2025;199:109204. https://doi.org/10.1016/j.compositesa.2025.109204.

[24] Duan Y, Liang Q, Yang Z, Wang X, Liu P, Li D. Ultrabroadband metastructure absorber with angular stability for conformal applications. Mater Today Phys 2023;39:101278. https://doi.org/10.1016/j.mtphys.2023.101278.

[25] Sun H, Zhang Y, Wu Y, Li C, Wei G, Wang J, Liu L, Tang S, Ji G. Broadband and high-efficiency microwave absorbers based on pyramid structure. ACS Appl Mater Interfaces 2022;14:52182–92. https://doi.org/10.1021/acsami.2c16166.

[26] Feng M, Zhang K, Cheng H, Li Y, Liu B, Liang B. A nanocomposite metamaterial with excellent broadband microwave absorption performance and good mechanical property. Compos Sci Technol 2023;239:110050. https://doi.org/10.1016/j.compscitech.2023.110050.

[27] Chen Z, Zhang Y, Wang Z, Wu Y, Zhao Y, Liu L, Ji G. Bioinspired moth-eye multi-mechanism composite ultra-wideband microwave absorber based on the graphite powder. Carbon 2023;201:542–8. https://doi.org/10.1016/j.carbon.2022.09.035.

[28] Feng M, Zhang K, Xiao J, Liu B, Cheng H, Li Y, Zhao Z, Liang B. Material-structure collaborative design for broadband microwave absorption metamaterial with low density and thin thickness. Composites, Part B Eng 2023;263:110862. https://doi.org/10.1016/j.compositesb.2023.110862.

[29] Mao Y, Sheng Y, Sun H, Yang C, Liu J, Wang Y, Zhang K, Tang C, Fu S. Multiscale structural engineering of cellulose-derived carbon aerogel metamaterials for broadband microwave absorption. Small 2026;22:e2512149. https://doi.org/10.1002/smll.202512149.

[30] Song WL, Zhou Z, Wang LC, Cheng XD, Chen M, He R, Chen H, Yang Y, Fang D. Constructing repairable meta-structures of ultra-broad-band electromagnetic absorption from three-dimensional printed patterned shells. ACS Appl Mater Interfaces 2017;9:43179–87. https://doi.org/10.1021/acsami.7b15367.

[31] Zhang T, Duan Y, Liu J, Pang H, Huang L, Ma X, Shi Y, Ma B. Polarization insensitive hierarchical metamaterial for broadband microwave absorption with multi-scale optimization and integrated design. Compos Sci Technol 2022;228:109643. https://doi.org/10.1016/j.compscitech.2022.109643.

[32] Huang B, Ye F, Liu Y, Liang J, Cao Y, Cheng L. Thin and ultra-broadband electromagnetic absorption carbonyl iron-based metamaterial via multiscale synergic dielectric-magnetic design. Compos Sci Technol 2024;250:110509. https://doi.org/10.1016/j.compscitech.2024.110509.

[33] Chen M, Wang L, Liu G, Liu T, Wang L, Li D, Tian X, Liang Q, Ge C. Multi-material continuous fiber reinforced metastructures: innovative design for enhanced broadband electromagnetic wave absorption and robust mechanical load-bearing. Composites, Part B Eng 2026;311:113190. https://doi.org/10.1016/j.compositesb.2025.113190.

[34] Li C, Gao Y, He X, Lai Y, Xie Y, Qi W, Man Q, Shen B. A novel strategy of magnetic-dielectric synergistic metamaterials based on multifunctional anisotropic aerogels for superior electromagnetic wave absorption. Chem Eng J 2025;522:167208. https://doi.org/10.1016/j.cej.2025.167208.

[35] Du L, Li Y, Zhou Q, Shi T, Zhang L, Wang J, Wang X, Fan X. A flexible metamaterial based on CNTs/Cellulose aerogels for broadband and ultra-lightweight microwave absorbers. Compos Sci Technol 2025;261:111024. https://doi.org/10.1016/j.compscitech.2024.111024.

[36] Ma W, Liu X, Yang T, Wang J, Qiu Z, Cai Z, Bai P, Ji X, Huang Y. Strong magnetic–dielectric synergistic gradient metamaterials for boosting superior multispectral ultra-broadband absorption with low-frequency compatibility. Adv Funct Mater 2024;34:2314046. https://doi.org/10.1002/adfm.202314046.

[37] Jiang B, Shang J, Li N, Wang Y, Hu Z, Yu J. Aramid honeycomb composites filled with rGO/BC aerogel for broadband microwave absorption and multifunctional applications. Compos Commun 2025:102512. https://doi.org/10.1016/j.coco.2025.102512.

[38] Huang H, Li S, Wu S, Wang J, Lu H, Xing L. In-situ synthesis of carbon black/polyvinyl alcohol aerogel-filled honeycomb structure via one-step freeze-drying for broadband microwave absorption and enhanced mechanical properties. J Alloys Compd 2022;905:164183. https://doi.org/10.1016/j.jallcom.2022.164183.

[39] Shi K, Li J, Wu Y, Bai H, Hong Y, Zhou Z. Lightweight composite microwave absorbing materials based on graphene aerogels with honeycomb structure. Phys Status Solidi RRL 2019;13:1900179. https://doi.org/10.1002/pssr.201900179.

[40] Sun H, Zhang M, Ji D, Ma C, Yuan B, Feng R, et al. Resin-free aramid honeycombs with extraordinary microwave absorption, thermal insulation, flame retardant and mechanical performance. J Mater Sci Technol 2025;233:132–43. https://doi.org/10.1016/j.jmst.2025.02.025.

[41] Wu H, Ren X, Hu W, Tang Y, Yin H, Fan H, Yuan H, Wang C, Xin Y. Permittivity controllable CNTs/PI composite aerogels with oriented microchannels for advanced microwave absorption and thermal isolation. Carbon 2025;233:119883. https://doi.org/10.1016/j.carbon.2024.119883.

[42] Cao X, Liu Y, Sun Q, Che T, Wu C, Yang Y. CNTs/PVA composite aerogel for efficient microwave and acoustic absorption. Compos Struct 2024;329:117805. https://doi.org/10.1016/j.compstruct.2023.117805.
[43] Yu C, Lin D, Guo J, Zhuang K, Yao Y, Zhang X, Jiang X. Ultralight three-layer gradient-structured MXene/reduced graphene oxide composite aerogels with broadband microwave absorption and dynamic infrared camouflage. Small 2024; 20:2401755. https://doi.org/10.1002/smll.202401755.
[44] Shen F, Long L, Cheng H, Liu H, Sun Y, Liu X. From intrinsic magnetic-dielectric double loss to circular truncated cone array structural absorber: dual strategies for ultra-broadband microwave absorption performances. Carbon 2024;216:118531. https://doi.org/10.1016/j.carbon.2023.118531.
[45] Yin L, Tian X, Cui C, Wang Z. A bioinspired helical metamaterial for broadband electromagnetic wave absorption. Composites, Part B Eng 2025;304:112685. https://doi.org/10.1016/j.compositesb.2025.112685.
[46] Bi Y, Ma M, Liao Z, Tong Z, Wang Y, Wu G, et al. Ultrabroad-band and low-frequency microwave absorption based on activated waxberry metamaterial. Chem Eng J 2021;426:131256. https://doi.org/10.1016/j.cej.2021.131256.
[47] Li S, Huang H, Wu S, Wang J, Xing L. Multilayer polyvinyl alcohol/carbon composite aerogels with broadband microwave and noise absorption and novel shape memory effect. ACS Appl Mater Interfaces 2021;13:56501–11. https://doi.org/10.1021/acsami.1c18286.
[48] Sun X, Li Y, Huang Y, Cheng Y, Wang S, Yin W. Achieving super broadband electromagnetic absorption by optimizing impedance match of rGO sponge metamaterials. Adv Funct Mater 2022;32:2107508. https://doi.org/10.1002/adfm.202107508.
[49] Fu W, Wu H, Liu S, Chao B, Deng K, Li Y. 3D-printed multi-material pyramids for broadband electromagnetic wave absorption. Mater Sci Eng B 2024;307:117525. https://doi.org/10.1016/j.mseb.2024.117525.
[50] Wang A, Zhang Z, Liu Y, Li Z, Leng J. Lightweight carbon nanotube/aramid nanofiber aerogel with superior electromagnetic wave absorption, thermal insulation, and flame resistance. Carbon 2024;225:119105. https://doi.org/10.1016/j.carbon.2024.119105.
[51] Qin M, Zhang L, Wu H. Dielectric loss mechanism in electromagnetic wave absorbing materials. Adv Sci 2022;9:2105553. https://doi.org/10.1002/advs.202105553.
[52] Qin Z, Ren Y, Yang S, Li P, Wang Z, Feng D, et al. Hierarchically porous N-doped dual-carbon coupled Co5.47N composite with tunable electromagnetic shielding and absorption properties. J Alloys Compd 2025;1010:177670. https://doi.org/10.1016/j.jallcom.2024.177670.
[53] Ren Y, Yang S, Xi T, Li P, Feng D, Bai Z, et al. Ascorbic acid-assisted construction of CoMoMOF derivative/rGO aerogel composites for electromagnetic shielding and microwave absorption. Compos Part A 2026;201:109423. https://doi.org/10.1016/j.compositesa.2025.109423.
[54] Ren Y, Qin Z, Xi T, Yang S, Du Z, Feng D, et al. Fe/Fe3O4/FexN@N-doped porous carbon aerogels with superior electromagnetic attenuation performance and multifunctional applications. Chem Eng J 2025;523:168786. https://doi.org/10.1016/j.cej.2025.168786.
[55] Qu N, Sun H, Sun Y, He M, Xing R, Gu J, Kong J. 2D/2D coupled MOF/Fe composite metamaterials enable robust ultra-broadband microwave absorption. Nat Commun 2024;15:5642. https://doi.org/10.1038/s41467-024-49998-y.
[56] Liu X, Si Z, Qian Y, Wu L, Xu X, Wan G, Wang G. Gradient-nested organic/inorganic aerogels achieve high mechanical strength and feedback-tunable microwave absorption. Research 2026;9:1074. https://doi.org/10.34133/research.1074.
[57] Ren J, Yin JY. 3D-printed low-cost dielectric-resonator-based ultra-broadband microwave absorber using carbon-loaded acrylonitrile butadiene styrene polymer. Materials 2018;11:1249. https://doi.org/10.3390/ma11071249.
[58] Tan R, Zhou F, Liu Y, Zhang B, Yang Y, Zhou J, Chen P, Jiang T. 3D printed propeller-like metamaterial for wide-angle and broadband microwave absorption. J Mater Sci Technol 2023;144:45–53. https://doi.org/10.1016/j.jmst.2022.10.012.
[59] Zhou Q, Du L, Duan W, Chen J, Yang Y, Shu C, Ye F, Fan X. Multiscale-engineered CNTs/cellulose@TPU aerogel with extended matching thickness for adaptive broadband microwave absorption. Compos Sci Technol 2026;275:111488. https://doi.org/10.1016/j.compscitech.2025.111488.
[60] Ge C, Dong H, Li Z, Yu C, Wang Z, Sun Y, Huang Y, Zhao T, Li Y, Wang L. Bioinspired 3D printed metamaterial for wideband microwave absorption and aerodynamic efficiency. Compos Sci Technol 2024;257:110846. https://doi.org/10.1016/j.compscitech.2024.110846.
[61] Wang X, Yuan Y, Wang L, Sun X, Zhang T, Liu C, Li Y. Intelligent design of multifunctional graphene-based aerogels for ultra-broadband microwave absorption. J Adv Ceram 2025;14:9221172. https://doi.org/10.26599/JAC.2025.9221172.